Sensors and Actuators A 279 (2018) 53–64

Contents lists available at ScienceDirect

Sensors and Actuators A: Physical

journal homepage: www.elsevier.com/locate/sna

Piezoelectric MEMS acoustic emission sensors

Minoo Kabir, Hanie Kazari, Didem Ozevin*

Department of Civil and Materials Engineering, University of Illinois at Chicago, 842 W Taylor Street ERF 2067, Chicago, IL 60607, USA

ARTICLE INFO

Article history:
Received 20 February 2018
Received in revised form 20 May 2018
Accepted 31 May 2018
Available online 1 June 2018

MSC:
00-01
99-00

Keywords:
Piezoelectric
MEMS
Acoustic emission
PiezoMUMPs

ABSTRACT

In this paper, piezoelectric MEMS (piezo-MEMS) sensors are designed and characterized for detecting elastic waves released by active flaws, known as acoustic emission (AE). The designed sensors operate in plate flexural mode or rigid body mode driven by the vibration of silicon diaphragm where piezoelectric layer is deposited on. The designed device contains two different frequency sensors tuned to 40 kHz and 200 kHz. The microstructural layers consist of doped silicon, aluminum nitride (AlN) and metal layer, which function as the bottom electrode, sensing layer and top electrode, respectively. The silicon layer also functions as a mass-spring system where a movable plate is connected with four partially clamped beams to the substrate. As the geometry sizes are restricted by the design rules of the manufacturing process, an additional mass is provided for the 40 kHz sensor through the substrate etching process. The sensors are numerically modeled using COMSOL Multiphysics software to obtain the frequency response and the dynamic response under excitation. Afterwards, the sensors are manufactured using Piezoelectric Multi-User MEMS Process (PiezoMUMPs) provided by MEMSCAP foundry. The performance of the designed sensors is demonstrated through electromechanical characterization experiments. A face-to-face response is obtained for each sensor, and the performance of the designed sensors is compared with the conventional piezoelectric AE sensors. The developed piezo-MEMS AE sensors have advantages of small foot-print, low cost and no need for bias voltage for operation.

1. Introduction

The acoustic emission (AE) is a nondestructive evaluation method to detect the presence of defects in a variety of structures, including bridges, aircrafts and pipelines [1–3]. The passive nature of this method provides real time data about the structural integrity and the presence of flaws. AE sensors are directly attached on the surface of a structure to detect and convert the elastic waves generated by an active defect into forms of electrical signals. The received signals are further analyzed to extract information about time, location, intensity and type of the defect [4–6]. Several advanced techniques are proposed in literature, such as source characterization and probabilistic framework, to supplementary interpret the data [7–9]. Primarily, the precise implementation of AE method depends on the detecting system, specifically, the performance and characteristics of the sensors. The AE sensors are conventionally made of bulky piezoelectric materials. These sensors generally operate in resonance mode, and are designed based on diameter and thickness of the piezoelectric material [10].

With the advancement of micromachining techniques, several studies have been reported on designing AE sensors based on micro-electro-mechanical systems (MEMS). The basic principle of MEMS AE and vibration sensors is similar: mass-damping-spring system in micro scale. While MEMS AE sensors operate at the resonant frequency of micro structure (typically tuned to 20 kHz and above), MEMS accelerometers operate below resonant frequency of micro structure (0–1000 Hz) in order to have linear relationship between input acceleration and output signal. For instance, Ozevin et al. [11] designed a MEMS device containing multiple capacitive resonant transducers, and experimentally demonstrated the ability of the transducers to detect AE events in crack initiation and growth. Their designed transducers consisted of a diaphragm moving above a fixed substrate, work with the mechanism of capacitance change between two parallel plates. In capacitive MEMS sensors, the deflection of the membrane, in the presence of a DC bias voltage, generates an output signal in a form of current. Moreover, directivity can be achieved through designing the moving electrodes in different directions. A 3-D AE sensor array was designed by Greve et al. [12] using PolyMUMPs process in which the array collocated two in-plane sensors with one out-of-plane sensor. Later, Saboonchi and Ozevin [13,14] designed and fabricated a MEMS device including a set of in-plane and out-of-plane sensors tuned to a range of frequencies between 60 and 200 kHz. They demonstrated that with the high aspect ratio geometry design, better sensitivity

* Corresponding author.
E-mail addresses: mkabir5@uic.edu (M. Kabir), hkazar2@uic.edu (H. Kazari), dozevin@uic.edu (D. Ozevin).

https://doi.org/10.1016/j.sna.2018.05.044
0924-4247/

and response characteristic can be achieved. The response characteristics and directional sensitivity of these sensors were assessed using laser excitation and in an actual crack growth monitoring of aluminum 7075 specimens under fatigue test [15,16]. The capacitive MEMS sensors have shown a great potential to be applied in the AE method; however, their major challenge in a field deployment is the requirement of high bias voltage. Unlike the capacitive MEMS sensors, the piezoelectric MEMS sensors are introduced, working with the transduction principle of piezoelectricity, which operate without bias voltage. Besides, they require lower polarization voltage, and need no gap to reach the desired transducer sensitivity. They are made of a thin-film of piezoelectric material, such as lead zirconate titanate (PZT), aluminum nitride (AlN) or zinc oxide (ZnO), sandwiched between two layers of electrodes through micromachining depositions [17,18]. Recently, the piezoelectric micromachined ultrasonic transducers (PMUTs) are investigated as an alternative to conventional piezocomposite ultrasonic transducers due to their unique features [19–21]. Various methods have been widely applied to study and characterize PMUTs. For instance, Feng et al. [22] presented a MEMS AE sensor with a cantilever sensing structure in which a layer of PZT was deposited on the cantilever for AE sensing. Sommer et al. [23] utilized modified high aspect ratio micromachining (HARM) technology to fabricate MEMS AE sensor working in the frequency range of 100–130 kHz. Lu et al. [24] denoted short-range and high resolution ultrasonic imaging using PMUTs array. Massimino et al. [25] applied complete multi-physics modeling using finite element method to verify the mechanical and acoustical responses for air-coupled PMUTs, which were tuned to 100 kHz resonant frequency. The numerical models considered the residual stress induced during fabrication process, and proper modeling of air along with coupling between different fields. In another study, Shelton et al. [26] produced 5×5 array of complementary metal-oxide-semiconductor (CMOS)-compatible PMUTs excited at 220 kHz resonant frequency by using AlN as the active piezoelectric layer.

In this study, the design and characterization of piezoelectric MEMS sensors are presented to detect acoustic emissions at two distinct frequency bands. The resonant AE sensors include low-frequency (LF) design tuned to 40 kHz and high-frequency (HF) design tuned to 200 kHz. The sensors are manufactured using PiezoMUMPs by MEMSCAP foundry. The PiezoMUMPs process is a 5-masks level SOI patterning and etching process, which includes deposition of 0.5 μm AlN to form piezoelectric layer [27]. First, the sensors are numerically modeled using COMSOL Multiphysics software to tune them for the desired resonance frequencies. The details of design and manufacturing steps, and the numerical results are presented in Section 2. Then, the fabricated sensors are packaged and the electrical connections are made through wire bonding. The performance of the piezo-MEMS AE sensors is demonstrated through electromechanical and mechanical characterization experiments in Section 3. In Section 4, the piezo-MEMS AE sensors are compared with the conventional piezoelectric AE sensors. Finally, the major outcomes of this study are summarized in Section 5.

2. Sensor design

2.1. Manufacturing process

The sensors are manufactured using the PiezoMUMPs provided by MEMSCAP foundry [27], in which thin-film piezoelectric devices are micromachined on a 150 mm (100) oriented silicon-on-insulator (SOI) wafer. The manufacturing process is described below as illustrated in Fig. 1, via the cross-sectional view of the device.

Table 1
Electrical and mechanical properties of two common piezoelectric materials (AlN and PZT).

Coefficient	$e_{31,f}$ (cm^{-2})	d_{33} (pm V^{-1})	d_{31} (pm V^{-1})	$e_{31,f}/\epsilon_0\epsilon_{33,f}$
AlN [27,31]	−1.05	3.9	2.78	−11.3
PZT [28–30]	−8 to −12	60–130	171–274	−7 to −1.8

(1) The top surface of the silicon layer is doped using n-type doping. A phosphosilicate glass (PSG) layer is deposited and annealed at 1050 °C in Argon (this layer is then removed through wet etching).
(2) A thermal oxide layer of 2000 Å is grown and lithographically patterned through a first level mask. The thermal oxide layer provides isolation between the SOI, the AlN and the pad-metal layers.
(3) A 0.5 μm of AlN is deposited over the wafer by reactive sputtering, and then lithographically patterned through a second level mask.
(4) The pad-metal layer is deposited. The layers of 20 nm of chrome and 1 μm of aluminum are deposited and patterned through a liftoff process. The pad-metals form the electrodes for electrical connections.
(5) In a fourth mask level, the silicon and the oxide layer are lithographically patterned and etched through deep reactive ion etching. A special recipe eliminates any undercutting of silicon layer when the etch reaches the buried oxide.
(6) A protection material made of polymide coat is provided to the top surface in order to hold the wafer together through subsequent trench etching.
(7) The substrate layer is lithographically patterned from the bottom using a fifth mask level. The bottom side oxide layer is removed using reactive ion etching, and deep reactive ion etching is used to etch completely the substrate layer.
(8) Finally, a dry etch process is used to strip the front side protection material. This process releases any mechanical structures in the silicon layer that are located over through-holes defined in the substrate layer.

2.2. Final sensor design

The sensing layer consists of a thin-film piezoelectric layer sandwiched between the pad metal layer and the doped silicon layer. In this study, AlN is used as the piezoelectric material with the electrical and mechanical properties as presented in Table 1 [27–31]. Here, $e_{31,f}$ is intrinsic effective piezoelectric coefficient, ε_0 is vacuum permittivity, $\varepsilon_{33,f}$ is relative dielectric coefficient and d_{33} and d_{31} are polarization coefficients caused by per unit of mechanical stress. The value of coefficient $e_{31,f}/\varepsilon_0\varepsilon_{33,f}$ for AlN is higher than PZT, so it is preferred for sensing applications [17]. The value of d_{31} for AlN is provided by MEMSCAP from the PiezoMUMPs Design handbook and value of d_{33} for AlN, and d_{33} and d_{31} for PZT are from references. Besides, the residual stresses are avoided through the deposition process, as AlN does not require annealing procedure. The design of piezoelectric MEMS device is controlled through the design rules provided by the PiezoMUMPs Design Handbook published by MEMSCAP Inc. as described in Section 2.1. While the thicknesses of the layers are restricted by the manufacturing process, the planar dimensions are flexible but bounded with the design rules. The dimensions are varied to tune the fundamental frequency to 40 kHz (for LF sensor) or 200 kHz (for HF sensor). The microstructural layers consist of doped silicon, AlN and metal layer which are working as the bottom electrode, sensing layer and top electrode, respectively. Each design consists of a mass-spring system where a movable plate is connected with four partially clamped beams to the substrate. The mass and stiffness are con-

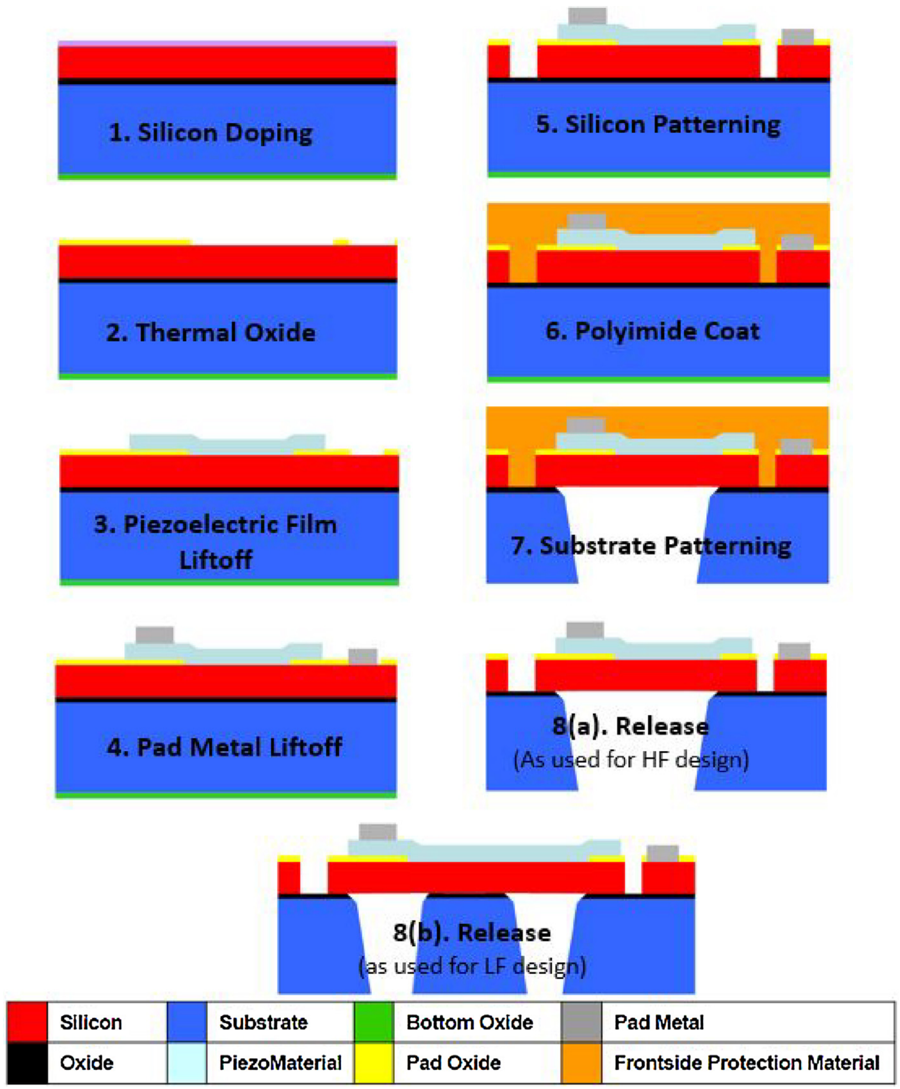

Fig. 1. Summary of the PiezoMUMPs [27].

trolled through the geometry of the beams and diaphragm to tune the sensors to the desired frequencies. For the design of the LF sensor, a reasonable beam and diaphragm geometry could not been achieved due to the restrictions of the design rules. Therefore, the back-surface etching is utilized for forming an additional mass to the doped silicon layer, which consists of entire silicon substrate. The cross-sectional views and dimensions of the sensors, deposited layers, etched areas as well as the planar view of the designed sensors in the L-Edit are presented in Fig. 2. The HF sensor operates in 31-mode where the applied stress in direction 3 is converted into the electrical voltage in direction 1. The LF sensor operates in 33-mode where the applied stress in direction 3 is converted into the electrical voltage in direction 3. The conversion mode is further discussed in the numerical studies section.

The scanning electron microscope (SEM) images of the piezo-MEMS sensors are presented in Fig. 3. The SEM images indicate successful etching process of the octagonal shape for both sensors and the large mass for the LF sensor.

2.3. Numerical studies

The main design variable is the resonant frequency of the sensors. The fundamental frequency of each sensor in z-direction is correlated to its modal stiffness and mass by the ratio of $\sqrt{k/m}$.

Table 2
Material properties of Si and AlN as used in numerical simulation.

Material	Density, ρ (kg m^{-3})	Young's modulus, E (GPa)	Poisson's ratio, ν
Si	2330	156	0.125
AlN	3300	320	0.24

The resonant frequency can be only adjusted by changing the length, width or the geometry of diaphragm and suspending mass, because the material properties and thickness of each layer are restricted by the fabrication process rules. The diaphragm and the suspending mass are simulated in COMSOL Multiphysics software implementing solid mechanics module. The eigenfrequency analysis is performed in order to find the fundamental mode shapes and frequencies. The thickness of the silicon layer is 10 μm while the thickness of the AlN and oxide layers are 0.5 μm and 1 μm, respectively. Since the thickness of the silicon layer is dominated in the entire device layers, only silicon layer is used in the models. The material properties of the silicon used in the numerical models are listed in Table 2.

Generally, a square shape diaphragm has higher fill factor; however, in terms of stress distribution, it does not have uniform stress specially at the edges where high stress concentration can be observed. Another geometric option is circular geometry. Based

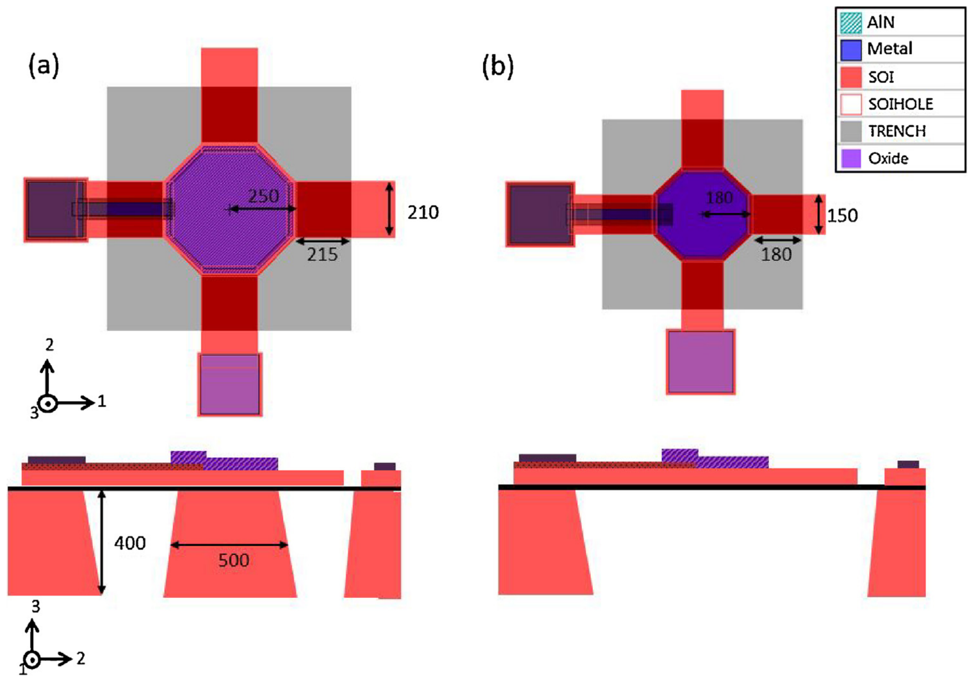

Fig. 2. L-Edit plots illustrating the planar view of the sensors designed for (a) 40 kHz (LF) and (b) 200 kHz (HF), along with the schematic cross-sectional view of each sensor (unit: μm).

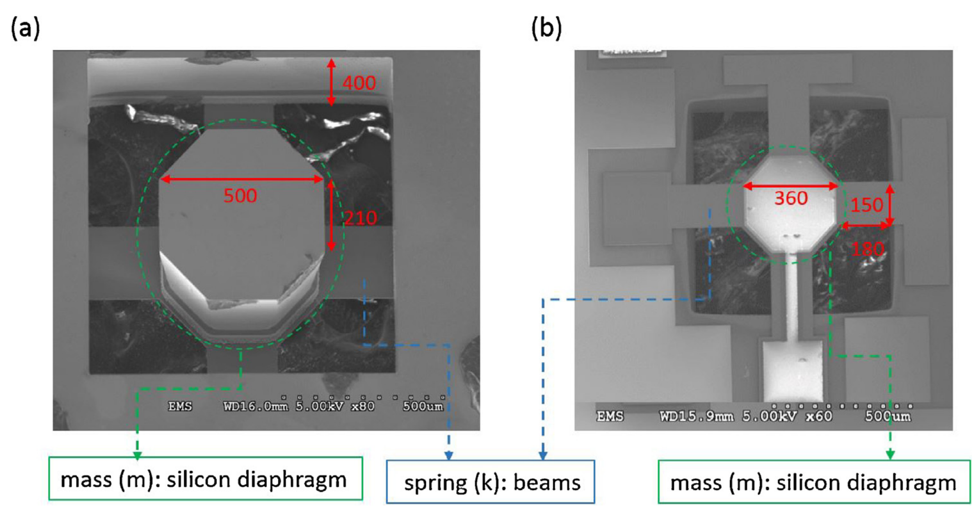

Fig. 3. SEM images of (a) LF and (b) HF sensors (unit: μm).

Table 3
Beams and octagonal dimensions.

Sensor	Beam dimensions (μm × μm)	Beam cross section (μm × μm)	Octagonal side (μm)
LF	210 × 215	10 × 210	210
HF	150 × 180	10 × 150	150

on the manufacturing design rules, there are restrictions in resolution of the circular shapes. An octagonal shape diaphragm is sought as the solution, as it is the closest polygon to circle and satisfies minimum beam dimensions of the design rules. The dimensions of the beams and octagonal shapes are listed in Table 3. To design the low frequency sensor, it is needed to have either lower beam stiffness or higher suspending mass. The highest possible size of the beams is restricted by the manufacturing design rules. Therefore, the lower frequency sensor is designed by increasing the suspending mass. The full thickness suspended structures can be defined through the substrate layer of the SOI wafer during the trench patterning procedure (step no. 7 of the manufacturing section). The full thickness suspended mass with octagonal shape is provided during the reactive-ion etching process. The thickness of the mass is the same as the substrate which is 400 μm. The fundamental frequencies of the LF and HF sensors obtained from the numerical simulations are presented in Fig. 4. Both the LF and HF designs are moving in *z*-direction with the fundamental frequencies of 40 kHz and 200 kHz, respectively. The second mode shapes of the sensors are presented as well, which are obtained as 41 kHz and 450 kHz for the LF and HF sensors, respectively. It is noticed that the first two modes of the LF sensor are close.

The second numerical model is conducted for the LF sensor using transient analysis in time domain to find the input–output conversion. The dynamic input signal is responded by the silicon diaphragm in the forms of inertial force, damping force and

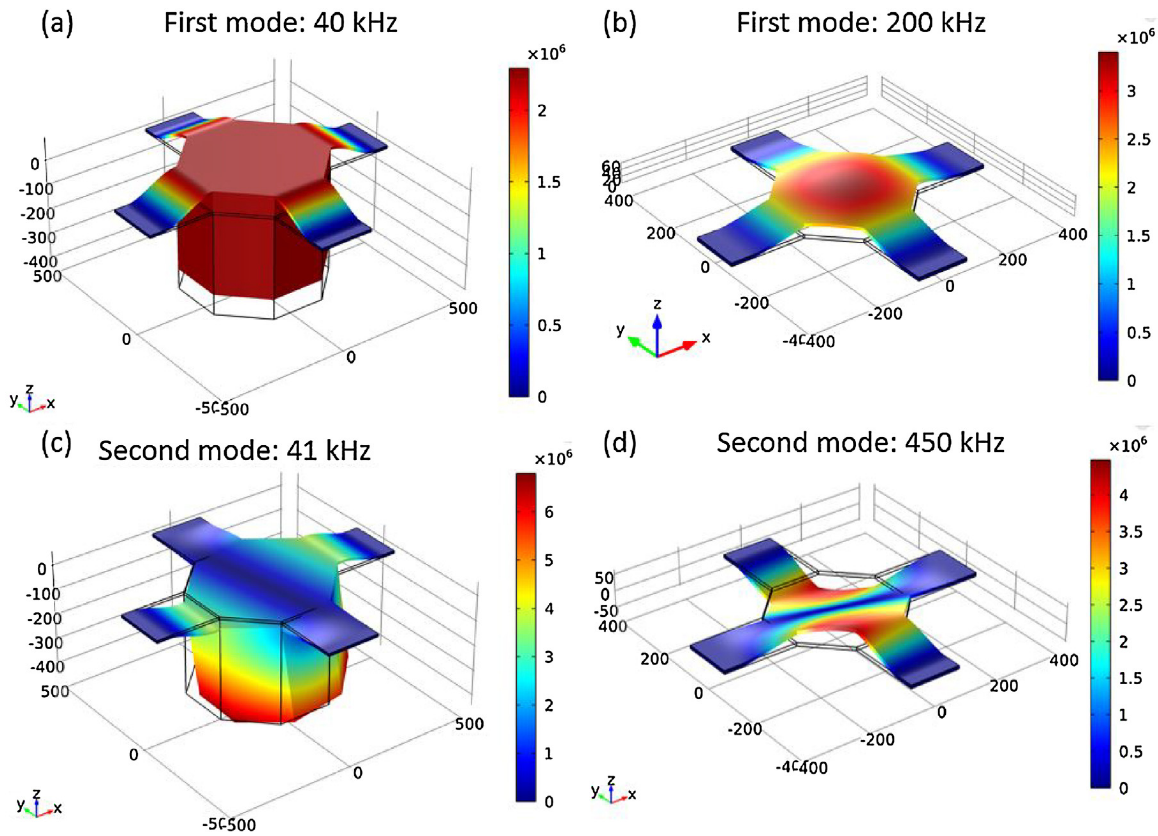

Fig. 4. The first and second mode shapes of (a, c) LF and (b, d) HF sensors.

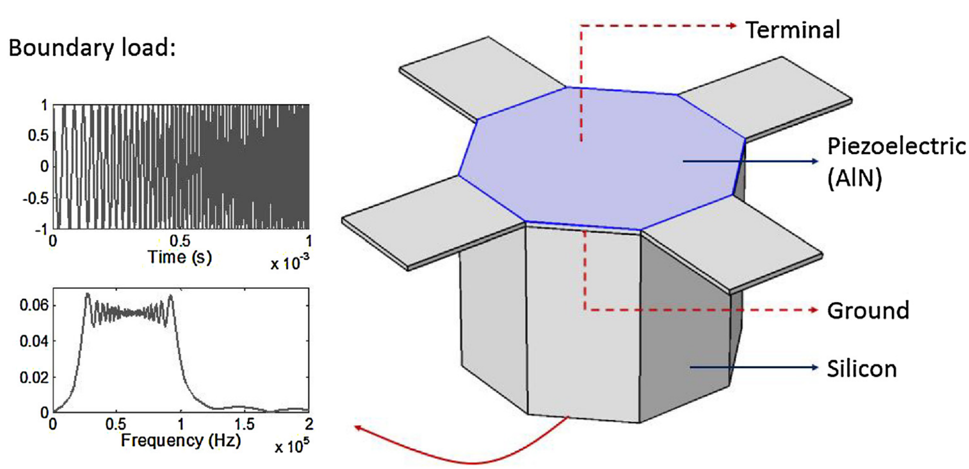

Fig. 5. The time-domain numerical simulation of the LF sensor, illustrating the defined AlN and silicon layers, the ground and terminal surfaces and the applied load.

spring force ($m\ddot{u}(t) + c\dot{u}(t) + ku(t) = F(t)$). The silicon diaphragm is coupled to piezoelectric layer, which then converts this internal dynamic strain into electrical signal by the electromechanical coupling response between strain-current of piezoelectric material. The constants (m, c and k) represent the micro structural properties of vibrating silicon diaphragm shown in Fig. 3. The packaged MEMS device is coupled to structure using couplant (e.g., vacuum grease) in order to transfer transient waves (from test structure to ceramic package and then to silicon diaphragm). The model uses the built-in piezoelectric device interaction in COMSOL, which contains two fundamental physics interfaces: solid mechanics and electrostatics. A thin layer of AlN (0.5 μm) is added on top of the silicon layer to simulate the piezoelectric domain. A wide-band load is introduced as a chirp signal, as the input mechanical force, which contains a range of frequencies from 10 kHz to 100 kHz. Free tetrahedral elements are used to mesh the model. The mesh resolution is kept at least 20 elements in one wavelength of the highest frequency to achieve acceptable accuracy [32]. The effect of damping is not considered in this study. Fig. 5 illustrates the piezoelectric layer, and the ground and terminal boundaries as defined on the bottom and top surfaces of the AlN. The input force and the output voltage received from the terminal layer and their frequency spectra are plotted in Fig. 6. It is observed that the output voltage has a narrow-band response at 40 kHz which confirms the designed frequency response of the LF sensor (Fig. 6(d)). Moreover, total displacement of the LF sensor at six different times in a typical cycle of

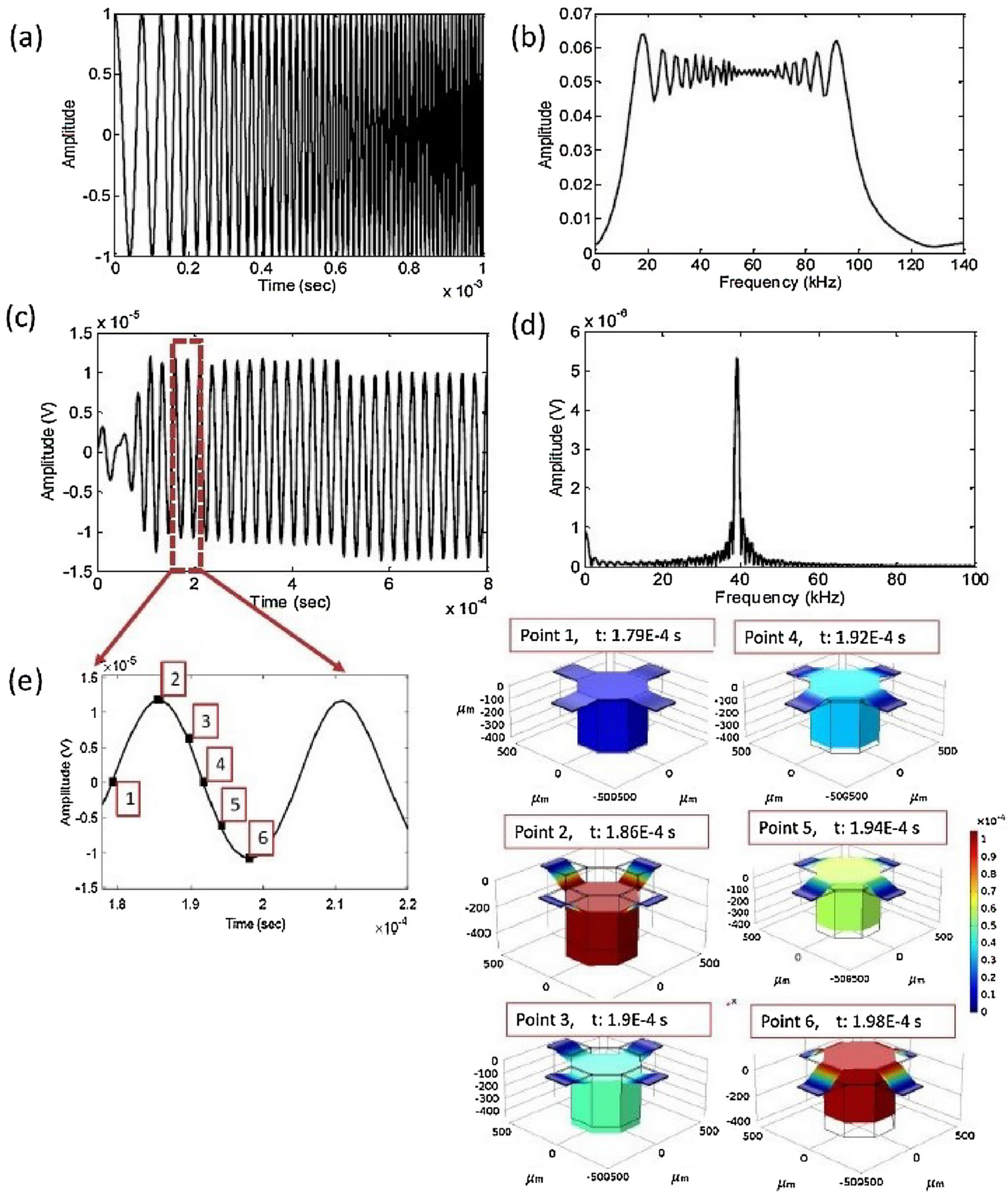

Fig. 6. Time-domain numerical analysis of the LF sensor, (a) the waveform of the applied chirp, (b) the frequency spectrum of the applied chirp signal, (c) the waveform of the received signal and (d) the frequency spectrum of the received signal, (e) the displaced shapes at six different time positions.

oscillation is shown in Fig. 6(e), which illustrates the out-of-plane movement of the sensor. It is worth noting that the movement of the LF sensor causes inertial force in the AlN layer, which is the main driving force leading to the production of current. There is no bending in the AlN layer as opposed to the diaphragm design of the HF sensor. The electric field polarization is parallel to the stress distribution in the AlN layer, as a result, the d_{33} mode should be considered for the LF sensor. The HF sensor converts mechanical movement into electrical current due to diaphragm deformation. The diaphragm is bended at the operational frequency (the curved shape is illustrated in the results of the eigenfrequency study), d_{31} is the piezoelectric conversion mode of the HF sensor.

3. Characterization experiments

The fabricated piezo-MEMS device is mounted on a ceramic package using a two-part silver epoxy, and the electrical connections are made through wire bonding. The packaged device is shown in Fig. 7(a). The MEMS chip contains four MEMS AE sensors that two of them are studied in this paper. The L-Edit image of the MEMS chip is used to illustrate the LF and HF sensors on the packaged device in Fig. 7(b), and the SEM image of the HF sensors is shown in Fig. 7(c). The electromechanical characterization of the packaged device is evaluated through measuring impedance, resistance, inductance, and passive and motional capacitances of the LF and HF sensors.

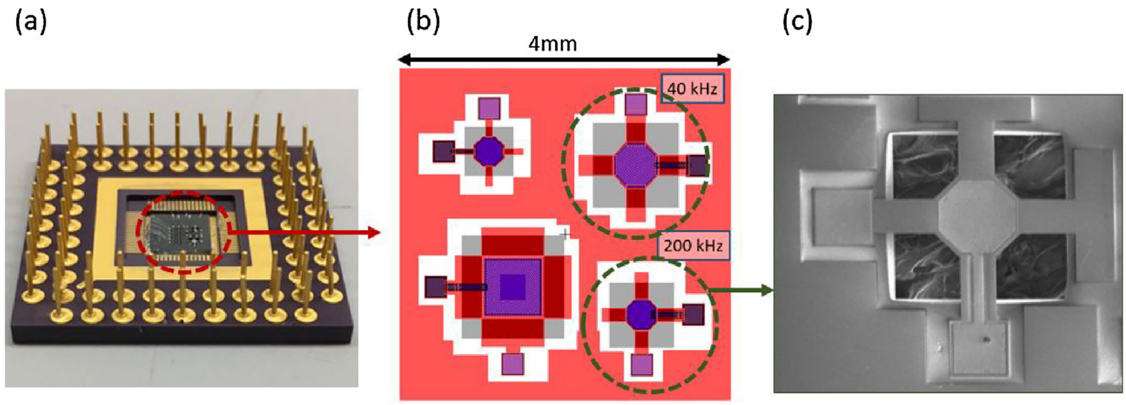

Fig. 7. (a) The packaged piezo-MEMS device (b) the L-Edit image of the MEMS chip that includes LF and HF sensors (c) the SEM image of the HF sensors.

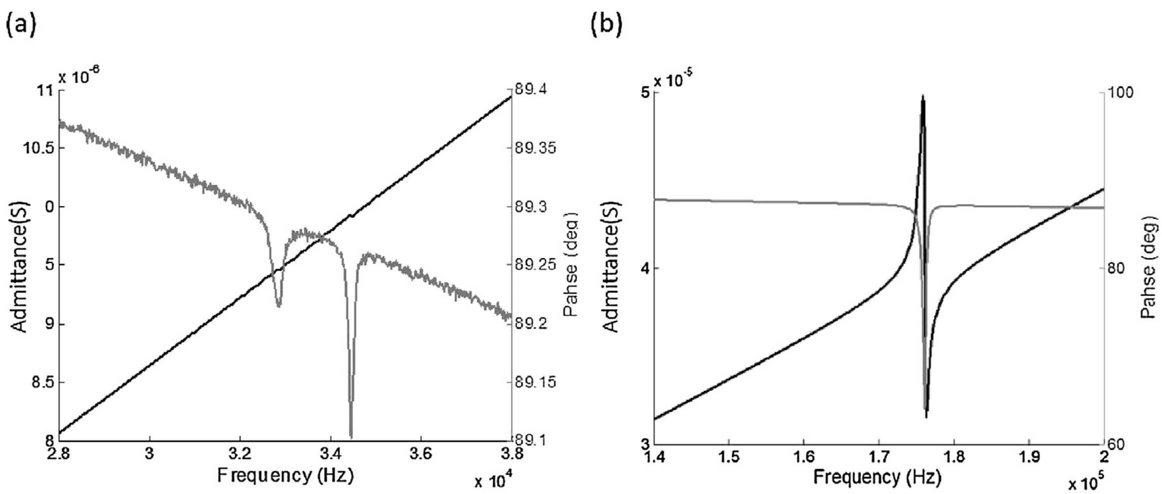

Fig. 8. Admittance results of the (a) LF and (b) HF sensors.

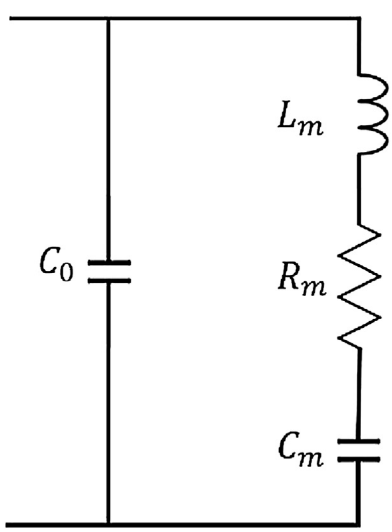

Fig. 9. Equivalent circuit model used to describe the electromechanical response of piezo-MEMS.

3.1. Electromechanical characterization

The main parameters to characterize piezo-MEMS are electrical and mechanical bandwidths and sensitivity. Here, effective coupling coefficient, K_{eff}, which is defined as the ratio of transduction between mechanical and electrical energy, is computed to evaluate the overall performance of the sensors. The admittance of each sensor is measured using impedance analyzer (Agilent Technologies, 4294A Precision Impedance Analyzer), by sweeping a range of frequencies. The measured admittance values, in the forms of magnitude and phase, are presented in Fig. 8. When the sweeping frequency matches the resonance frequency of the sensor, the impedance is amplified due to electromechanical coupling. The measured resonant frequencies along with the numerical resonant frequencies are tabulated in Table 4. The LF sensor as observed in the phase plot (Fig. 8) has two peaks. This is correlated with the fact that the first two modes of vibration of the LF design are close, as observed in the numerical simulation (Fig. 4(c)).

Table 4
Experimental and numerical resonant frequencies.

Sensor	Experimental (kHz)	Numerical (kHz)
LF	35	40
HF	175	200

In this study, the equivalent circuit as shown in Fig. 9 is utilized to represent the parameters to evaluate the electromechanical performance of the fabricated piezo-MEMS AE sensors [33]. The required components, including passive capacitance C_0, motional capacitance C_m, motional inductance L_m and motional resistance R_m are measured using impedance analyzer. The measured C_0 and C_m for the LF sensors are both 4.59×10^{-11} F, and for the HF sensor are 3.61×10^{-11} F and 4.76×10^{-11} F, respectively. The K_{eff} coeffi-

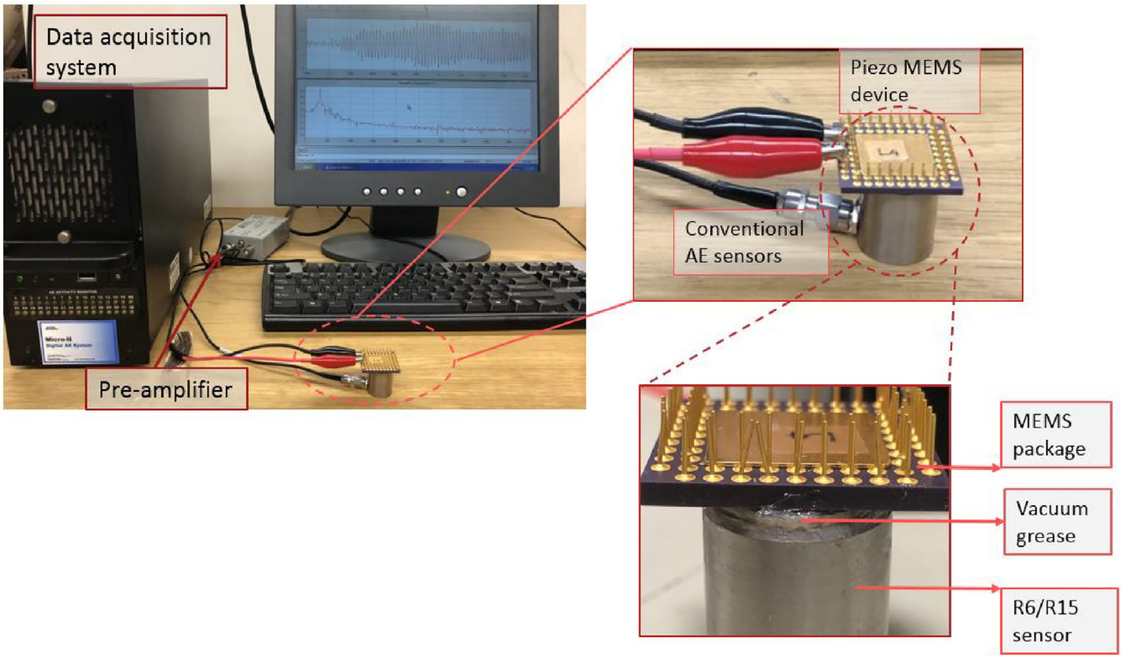

Fig. 10. Experimental setup for mechanical characterization of the LF and HF sensors using face-to-face excitation by conventional AE transducers.

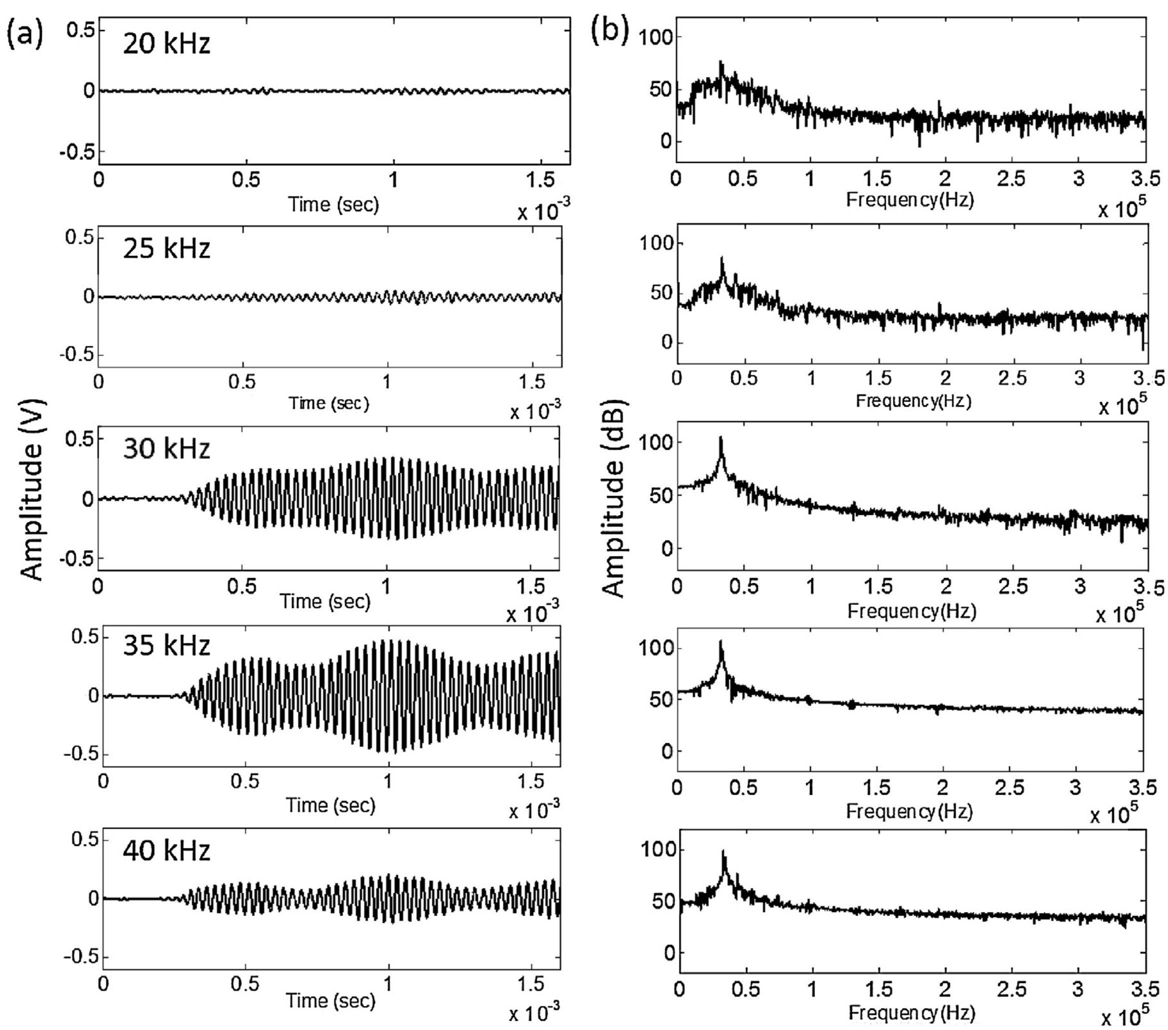

Fig. 11. The LF sensor responses at different excitation frequencies (a) time history signals and (b) their frequency spectra.

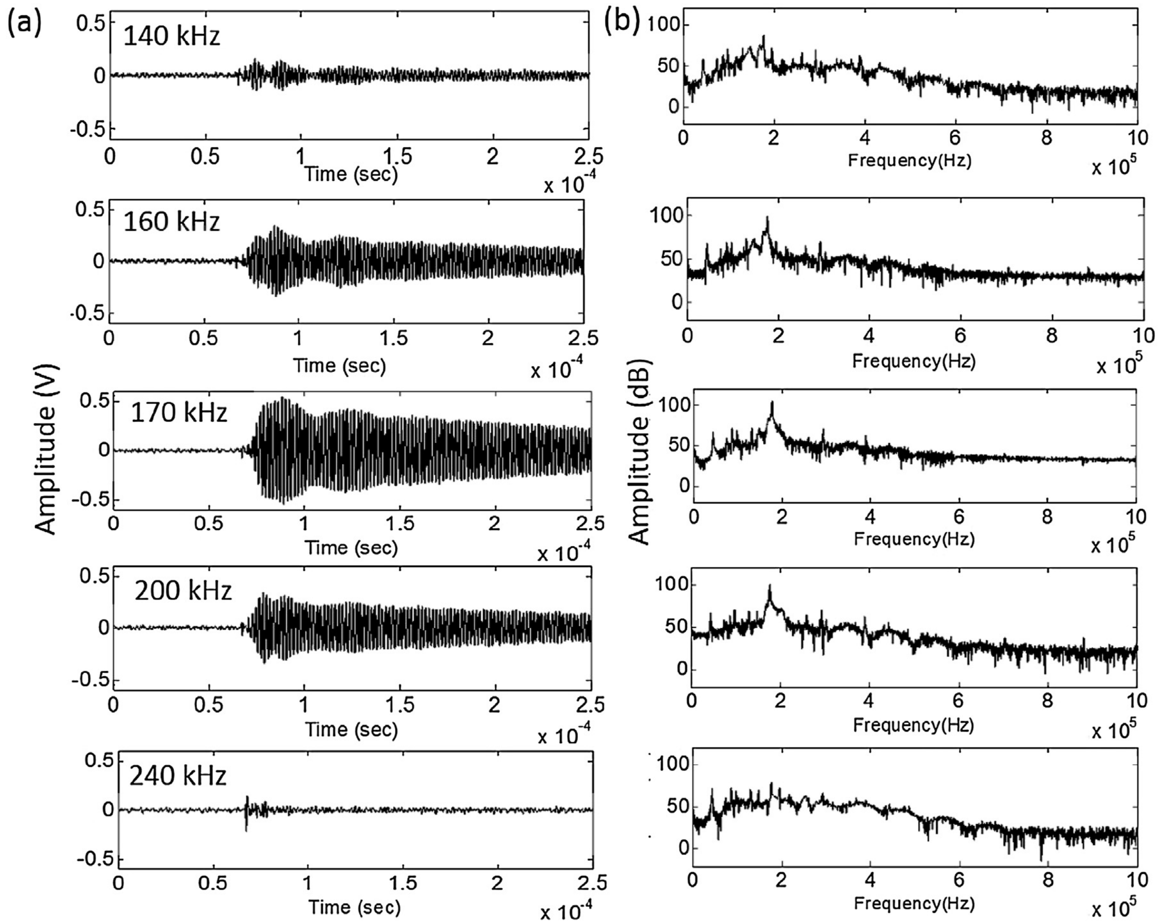

Fig. 12. The HF sensor responses at different excitation frequencies (a) time history signals and (b) their frequency spectra.

cient is correlated to the electrical and mechanical parameters by the following relation [33]

$$K_{eff}{}^2 = \frac{C_m}{C_m + C_0} \quad (1)$$

The value of K_{eff} is calculated as 75.4% for the HF sensor and 70% for the LF sensor. Another important parameter in MEMS resonators is *Q*-Factor, which is defined as the ratio of energy stored in the system to energy dissipated per cycle, and measured by the impedance analyzer. The *Q*-Factor values are measured as 71 and 1.98 for the LF and the HF, respectively. High *Q*-Factor for the LF sensor indicates a very low damping ratio.

3.2. Mechanical characterization

The performance of the sensors is studied using an excitation signal from the conventional piezoelectric transducer R6 or R15. R6 and R15 are resonant type piezoelectric AE transducers made of bulky piezoelectric ceramics. They have resonant frequencies at 60 kHz and 150 kHz, respectively, and are manufactured by Mistras Group Inc. The MEMS package is directly attached to the surface of the R6 and R15 transducers to excite the out-of-plane motion of the piezoelectric layers of the LF and HF sensors, respectively, using vacuum grease as the couplant. The experimental setup is shown in Fig. 10, with the close-up picture that shows the coupling of the MEMS package to the surface of the R6/R15 sensor using vacuum grease. The sensors are connected to the AE data acquisition system manufactured by Mistras Group Inc., and a built-in software (WaveGen 1410) is used to generate a 5-cycle sine wave with the desired frequency, and applying input voltage of 10 V. First, the R6 transducer is used for generating the excitation signal ranged from 10 kHz to 40 kHz with the increments of 1 kHz, and the LF sensor is used to receive the signal. Then, the R15 transducer is used for generating the excitation signal ranged from 120 kHz to 220 kHz with the increments of 5 kHz, and the HF sensor is used to receive the signals. The sampling frequencies are set as 1 MHz and 3 MHz for the LF and HF sensor experiments, respectively. The time domain signals along with their frequency spectra for the selected excitation frequencies near the resonant frequency of each sensor are presented in Figs. 11 and 12 for the LF and HF sensors, respectively. More cycles than excitation signal are observed in the time history signals due to low damping and multiple reflections of excitation signal. The maximum amplitudes of the time history from all the received signals are extracted and plotted in Fig. 13. The maximum amplitude of each sensor is near the designed resonant frequency, which is about 32 kHz for the LF sensor and 170 kHz for the HF sensor, similar to the electrochemical results as shown in Table 4. The LF sensor has very narrow bandwidth, which is important to apply the advanced source localization algorithms [6,34]. As obtained by the electromechanical experiments, the LF sensor has higher *Q*-factor (i.e. lower damping) than the HF sensor. However, the low damping of the LF sensor causes significant ringing, which may interfere with the AE signals released by short time differences.

4. The comparison of conventional piezoelectric and piezo-MEMS AE sensors

The behaviors of conventional piezoelectric and the designed piezo-MEMS AE sensors are compared under the same excitation signal generated on a plate-like structure. The LF sensor is com-

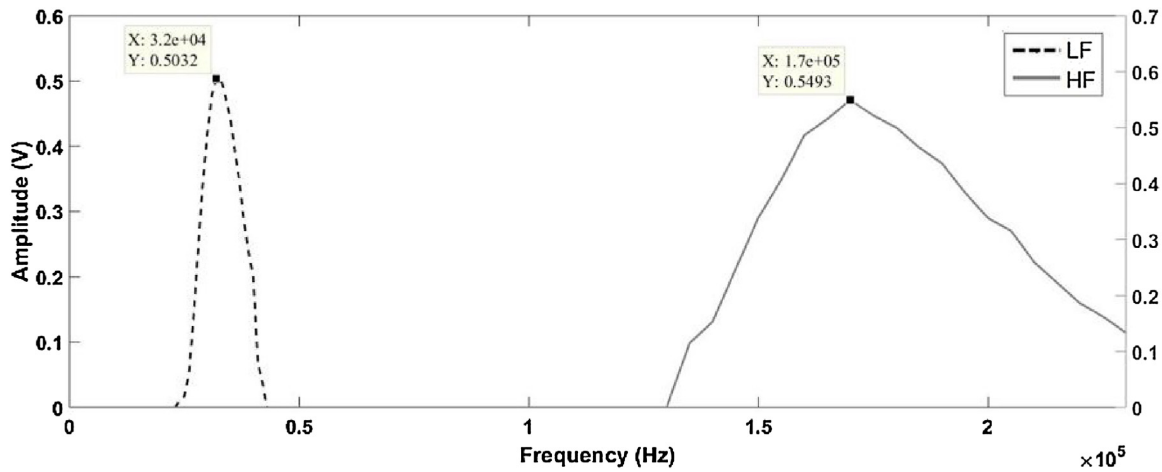

Fig. 13. The peak amplitudes of time history signals due to different excitation frequencies.

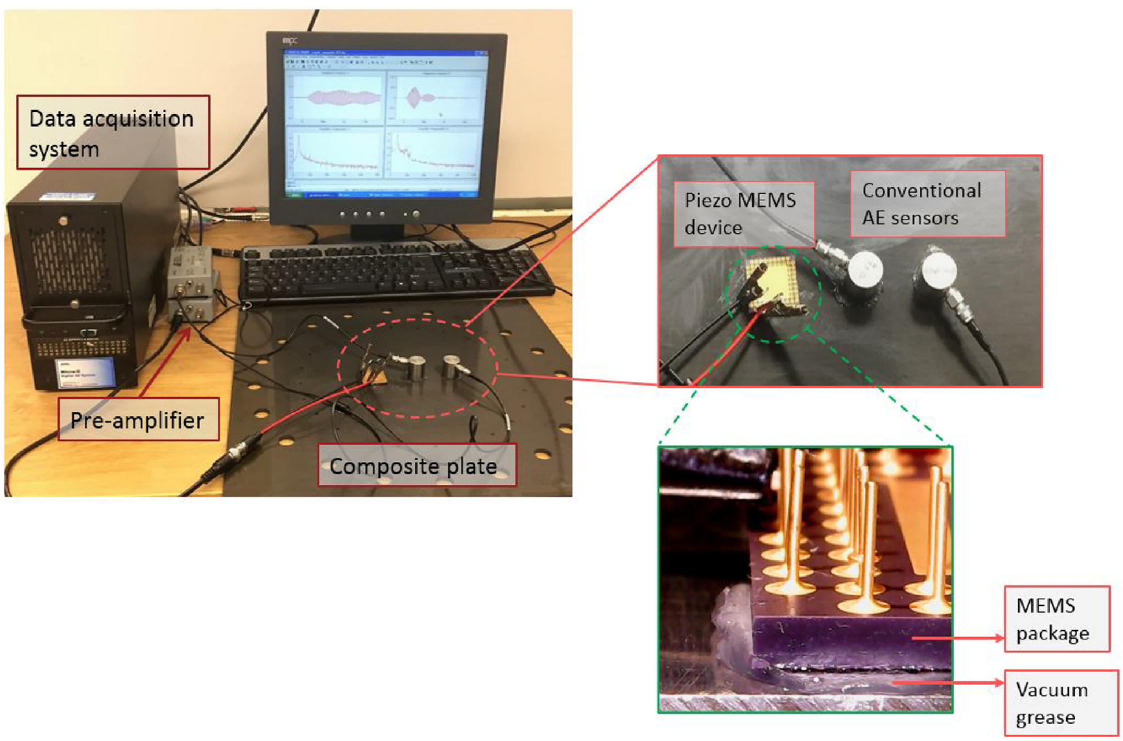

Fig. 14. Experimental setup for the comparison of conventional piezoelectric AE sensors and piezo-MEMS AE sensors.

pared with the R6 sensor using an excitation at 30 kHz. The sensors are attached to the surface of a composite plate with thickness of 5 mm using vacuum grease and connected to the AE data acquisition system using a 40 dB pre-amplifier, as shown in Fig. 14. Another R6 transducer is used to excite a 5-cycle sine wave signal at the frequency of 30 kHz. The same experiment is repeated for the HF and R15 sensors using another R15 transducer to generate the excitation signal near 170 kHz. The time history waveforms and their frequency spectra are presented in Fig. 15. The shapes of signals in both conventional piezoelectric and piezo-MEMS AE sensors are similar; however, the amplitudes of the received signals by the conventional piezoelectric AE sensors are two orders of magnitude higher than the piezo-MEMS AE sensors. Additionally, low damping of LF sensor causes reverberation, which decreases the decay time of AE signal and increases the waveform duration. However, it is important to note that a unit cell sensor is utilized to design each piezo-MEMS AE sensor. For example, the size of the LF sensor is about 1 mm × 1 mm. The sensitivity of the piezo-MEMS sensors can be improved by coupling a number of unit cells. The coupling of about 100 LF sensors, in a 10 × 10 array (1 cm^2 area), is sufficient to reach to the sensitivity of conventional piezoelectric AE sensors. The comparison of conventional piezoelectric and piezo-MEMS AE sensors including their dimensions is summarized in Table 5 in which thickness includes the packaging of each sensor as well, and total size represents total volume. The comparison of the amplitude/size as shown in Table 5 indicates that the HF sensor has superior behavior as compared to the conventional piezoelectric AE sensor.

5. Conclusions

In this study, the piezo-MEMS AE sensors are developed using piezoMUMPs provided by MEMSCAP, which have advantage over the capacitive type MEMS AE sensors due to no DC power require-

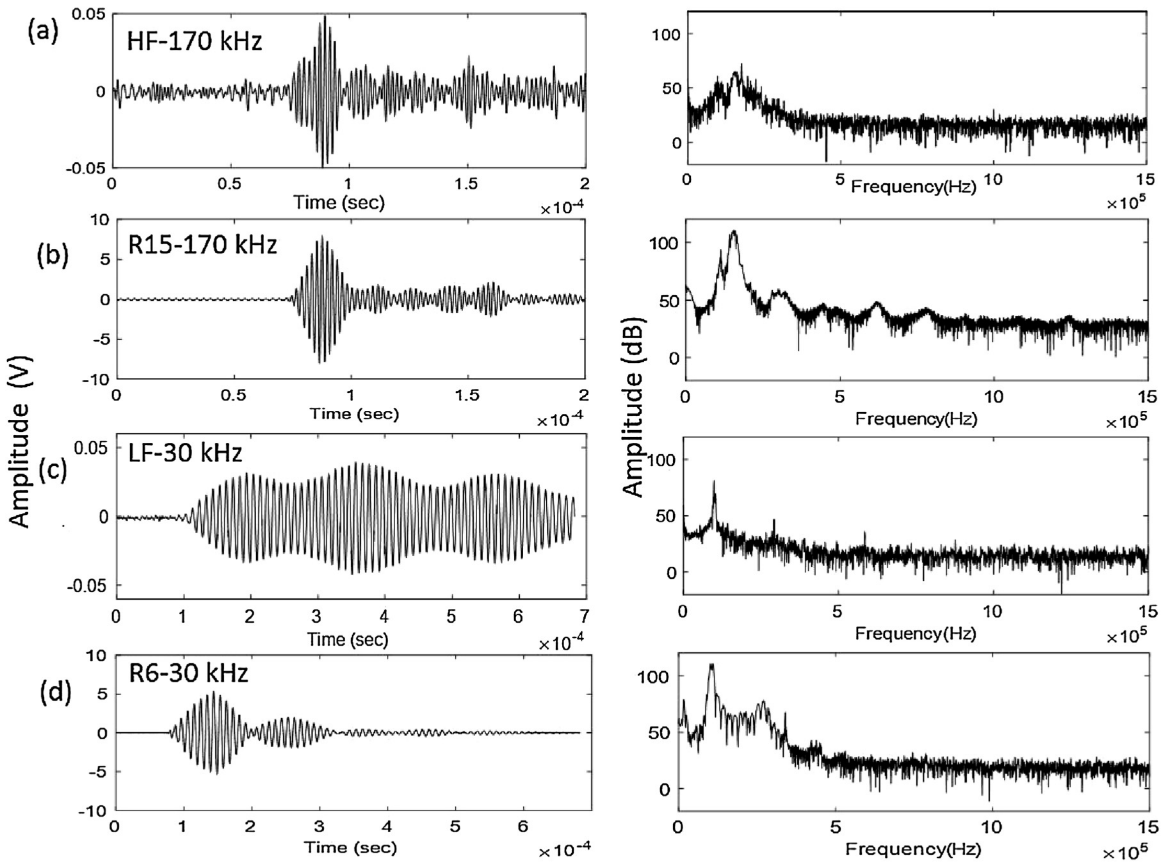

Fig. 15. The time history signals and their frequency spectra obtained from (a) HF (piezo-MEMS AE sensor), (b) R15 (conventional AE sensor), (c) LF (piezo-MEMS AE sensor), (d) R6 (conventional AE sensor).

Table 5
The comparison of conventional piezoelectric and piezo-MEMS AE sensors.

Sensor	Diameter/ width (mm)	Thickness (mm)	Total size (mm^3)	Maximum signal amplitude (V)	Amplitude/size (mV/mm^3)
R6	19.05	22.35	6373	5.368	0.84
LF	0.9	1	0.81	0.039	48.51
R15	19.05	22.35	6373	7.939	1.24
HF	0.7	1	0.49	0.048	99.59

ment to operate. The MEMS device contains two sensors with the design resonant frequencies of 40 kHz (LF sensor) and 200 kHz (HF sensor). The LF sensor is uniquely designed with a mass of entire silicon substrate in order to reduce the overall size of sensor while tuning it to lower frequency. However, the first two modes of vibration of the LF sensors are close, as observed in the numerical models and electromechanical experiments. The numerical simulation of the LF sensor in time-domain demonstrates the narrowband response of the sensor at the designed frequency, as well as the out-of-plane motion of the sensor. It is observed that no bending occurs in the AlN layer of the LF sensor. As a result, it is concluded that the development of inertial force causes the conversion of mechanical signal into electrical current. The electric field polarization is parallel to the stress distribution in the AlN layer of the LF sensor and d_{33} mode is the dominant mode of piezoelectric conversion. The diaphragm motion is the driving force of the HF sensor, as a result, d_{31} is the dominant mode of piezoelectric conversion.

The LF sensor demonstrates high Q-factor, leading to low damping and very narrow frequency bandwidth, which is important for source localization, especially in dispersive medium where wave velocity depends on frequency. The electrical and mechanical characterization experiments indicate an acceptable performance of the designed sensors. The sensitivities of piezo-MEMS sensors taking into account their sizes are comparable to conventional piezoelectric sensors. To increase the sensitivity of the designed piezo-MEMS AE sensors, a group of 100 unit cells can be connected in a 10 × 10 array (occupying 1 cm^2 area) to reach to the sensitivity of conventional AE sensors.

Acknowledgements

This investigation was supported by UI Labs DMDII Contract Number 0220160026 and the project title of “Intelligent Welding: Real Time Monitoring, Diagnosis, Decision and Control using Multi-sensor and Machine Learning” and National Science Foundation under Award No. CMMI 1552375 entitled “CAREER: Engineered Spatially Periodic Structure Design Integrated with Damage Detection Philosophy”. The support from the sponsoring organizations is gratefully acknowledged. Any opinions, findings, and conclusions or recommendations expressed in this paper are those of the authors and do not necessarily reflect the views of the organizations acknowledged above.

References

[1] A. Nair, C. Cai, Acoustic emission monitoring of bridges: review and case studies, Eng. Struct. 32 (6) (2010) 1704–1714.
[2] W. Staszewski, C. Boller, G.R. Tomlinson, Health Monitoring of Aerospace Structures: Smart Sensor Technologies and Signal Processing, John Wiley & Sons, 2004.
[3] R. Miller, A. Pollock, D. Watts, J. Carlyle, A. Tafuri, J. Yezzi, A reference standard for the development of acoustic emission pipeline leak detection techniques, NDT & E Int. 32 (1) (1999) 1–8.

[4] Z. Nazarchuk, V. Skalskyi, O. Serhiyenko, Acoustic Emission: Methodology and Application, Foundations of Engineering Mechanics, Springer International Publishing, 2017 https://books.google.com/books?id=eEgNvgAACAAJ.
[5] M. Kabir, H. Saboonchi, D. Ozevin, Accurate source localization using highly narrowband and densely populated MEMS acoustic emission sensors, Struct. Health Monit. (2015).
[6] A. Ebrahimkhanlou, S. Salamone, Acoustic emission source localization in thin metallic plates: a single-sensor approach based on multimodal edge reflections, Ultrasonics 78 (2017) 134–145.
[7] K. Ono, Structural integrity evaluation using acoustic emission, J. Acoust. Emiss. 25 (2007) 1–20.
[8] A. Ebrahimkhanlou, S. Salamone, A probabilistic framework for single-sensor acoustic emission source localization in thin metallic plates, Smart Mater. Struct. 26 (9) (2017) 095026.
[9] E. Nazarian, T. Taylor, T. Weifeng, F. Ansari, Machine-learning-based approach for post event assessment of damage in a turn-of-the-century building structure, J. Civ. Struct. Health Monit. 8 (2) (2018) 237–251, http://dx.doi.org/10.1007/s13349-018-0275-6.
[10] C.U. Grosse, M. Ohtsu, Acoustic Emission Testing, Springer Science & Business Media, 2008.
[11] D. Ozevin, D. Greve, I. Oppenheim, S. Pessiki, Resonant capacitive MEMS acoustic emission transducers, Smart Mater. Struct. 15 (6) (2006) 1863.
[12] D.W. Greve, I.J. Oppenheim, W. Wu, A.P. Wright, Development of a MEMS acoustic emission sensor system, Proc. of SPIE, vol. 6529 (2007) 652912-1.
[13] H. Saboonchi, D. Ozevin, MEMS acoustic emission transducers designed with high aspect ratio geometry, Smart Mater. Struct. 22 (9) (2013) 095006.
[14] H. Saboonchi, D. Ozevin, M. Kabir, MEMS sensor fusion: acoustic emission and strain, Sens. Actuators A: Phys. 247 (2016) 566–578.
[15] M. Kabir, H. Saboonchi, D. Ozevin, The design, characterization, and comparison of mems comb-drive acoustic emission transducers with the principles of area-change and gap-change, in: SPIE Smart Structures and Materials + Nondestructive Evaluation and Health Monitoring, International Society for Optics and Photonics, 2015, p. 94352B.
[16] M. Kabir, H. Saboonchi, D. Ozevin, Accurate source localization using highly narrowband and densely populated MEMS acoustic emission sensors, Struct. Health Monit. (2015).
[17] J. Jung, W. Lee, W. Kang, E. Shin, J. Ryu, H. Choi, Review of piezoelectric micromachined ultrasonic transducers and their applications, J. Micromech. Microeng. 27 (11) (2017) 113001.
[18] Z. Hao, B. Liao, An analytical study on interfacial dissipation in piezoelectric rectangular block resonators with in-plane longitudinal-mode vibrations, Sens. Actuators A: Phys. 163 (1) (2010) 401–409.
[19] F. Akasheh, T. Myers, J.D. Fraser, S. Bose, A. Bandyopadhyay, Development of piezoelectric micromachined ultrasonic transducers, Sens. Actuators A: Phys. 111 (2–3) (2004) 275–287.
[20] L.L. Wong, S. Na, A.I. Chen, Z. Li, M. Macecek, J.T. Yeow, A feasibility study of piezoelectric micromachined ultrasonic transducers fabrication using a multi-user MEMS process, Sens. Actuators A: Phys. 247 (2016) 430–439.
[21] Y. Wang, H. Ding, X. Le, W. Wang, J. Xie, A MEMS piezoelectric in-plane resonant accelerometer based on aluminum nitride with two-stage microleverage mechanism, Sens. Actuators A: Phys. 254 (2017) 126–133.
[22] G.-H. Feng, W.-M. Chen, Micromachined lead zirconium titanate thin-film-cantilever-based acoustic emission sensor with poly (n-isopropylacrylamide) actuator for increasing contact pressure, Smart Mater. Struct. 25 (5) (2016) 055046.
[23] R. Sommer, M. Freitag, J. Schaufuss, A. Sorger, J. Mehner, Improved MEMS AE sensors in harm technology, in: 2014 11th International Multi-Conference on Systems, Signals & Devices (SSD), IEEE, 2014, pp. 1–4.
[24] Y. Lu, H.-Y. Tang, S. Fung, B.E. Boser, D.A. Horsley, Pulse-echo ultrasound imaging using an aln piezoelectric micromachined ultrasonic transducer array with transmit beam-forming, J. Microelectromech. Syst. 25 (1) (2016) 179–187.
[25] G. Massimino, L. D'Alessandro, F. Procopio, R. Ardito, M. Ferrera, A. Corigliano, Air-coupled PMUT at 100 kHz with PZT active layer and residual stresses: multiphysics model and experimental validation, in: 2017 18th International Conference on Thermal, Mechanical and Multi-Physics Simulation and Experiments in Microelectronics and Microsystems (EuroSimE), IEEE, 2017, pp. 1–4.
[26] S. Shelton, M.-L. Chan, H. Park, D. Horsley, B. Boser, I. Izyumin, R. Przybyla, T. Frey, M. Judy, K. Nunan, et al., CMOS-compatible AlN piezoelectric micromachined ultrasonic transducers, in: 2009 IEEE International Ultrasonics Symposium (IUS), IEEE, 2009, pp. 402–405.
[27] A. Cowen, G. Hames, K. Glukh, B. Hardy, PiezoMUMPs Design Handbook, revision 1.3 ed., MEMSCAP Inc., 2014.
[28] N. Setter, D. Damjanovic, L. Eng, G. Fox, S. Gevorgian, S. Hong, A. Kingon, H. Kohlstedt, N. Park, G. Stephenson, et al., Ferroelectric thin films: review of materials, properties, and applications, J. Appl. Phys. 100 (5) (2006) 051606.
[29] M.-A. Dubois, P. Muralt, Properties of aluminum nitride thin films for piezoelectric transducers and microwave filter applications, Appl. Phys. Lett. 74 (20) (1999) 3032–3034.
[30] E. Alper, D.J. Inman, Piezoelectric Energy Harvesting, John Wiley & Sons, April 2011.
[31] M. Zhang, J. Yang, C. Si, G. Han, Y. Zhao, J. Ning, Research on the piezoelectric properties of aln thin films for mems applications, Micromachines 6 (9) (2015) 1236–1248.
[32] A. Mostavi, M. Kabir, D. Ozevin, The integration of superlattices and immersion nonlinear ultrasonics to enhance damage detection threshold, Appl. Phys. Lett. 111 (20) (2017) 201905.
[33] H. Choi, J. Ding, A. Bandyopadhyay, M. Anderson, S. Bose, Characterization and modeling of a piezoelectric micromachined ultrasonic transducer with a very large length/width aspect ratio, J. Micromech. Microeng. 18 (2) (2008) 025037.
[34] A. Ebrahimkhanlou, S. Salamone, Single-sensor acoustic emission source localization in plate-like structures: a deep learning approach, Proc. SPIE 10600 (2017) 10600–10600-9, http://dx.doi.org/10.1117/12.2296613.

Biographies

Minoo Kabir was received the B.Sc. and M.S. degrees from Sharif University of Technology in 2011 and 2013, respectively. She is currently a Ph.D. candidate in Civil and Materials Engineering at University of Illinois at Chicago since 2014. Her research interest includes MEMS sensors, and phononic materials for structural monitoring.

Hanie Kazari was received the B.Sc. degree from University of Tehran in 2016. She is currently a Ph.D. candidate in Civil and Materials Engineering at University of Illinois at Chicago since 2016. Her research interest includes MEMS sensors, additive manufacturing and structural monitoring.

Didem Ozevin received the B.Sc. and M.S. degrees from Bogazici University in Turkey and the Ph.D. degree from Lehigh University Bethlehem PA in 1997, 2000 and 2005, respectively. She is currently an associate professor of Civil and Materials Engineering Department, University of Illinois at Chicago, Chicago IL. Her current research interests include MEMS sensors for Structural Health Monitoring, acoustic emission, nonlinear ultrasonics and damage algorithm development. Her research includes both experimental and modeling components. She has more than five years of industrial research experience on nondestructive evaluation of structures.